RSC Advances

PAPER

View Article Online
View Journal | View Issue

Cite this: *RSC Adv.*, 2024, **14**, 12650

In situ one step growth of amorphous tin oxide electron transport layer for high-performance perovskite solar cells†

Wenlin Du, Zhe Wan, Jingyi Zhu, Xin Liu, Li Chen, Shuxia Li, Ning Kang * and Chenglong Wang*

Received 5th March 2024
Accepted 14th April 2024

DOI: 10.1039/d4ra01724b

rsc.li/rsc-advances

Tin oxide used in electron transport layer (ETL) exhibits key role in transmitting electrons and blocking holes in perovskite solar cells (PSCs) device. However, crystal tin oxide nanoparticles (NPs) become necessary to form SnO_2 film by method of spin-coating, resulting in possible surface defect and cracks among SnO_2 NPs, corresponding to unsatisfied performance PSCs. Herein, an amorphous tin oxide thin film is creatively *in situ* grew onto Fluorine-doped Tin Oxide (FTO) substrate as ETL. The designed solar cell device with structure of FTO/SnO_2/$MAPbI_3$/Sprio-OMeTAD/Ag owns a champion photoelectric conversion efficiency (PCE) up to 17.64%, 76.20% of filling coefficient (FF), and 1.09 V of open-circuit voltage (V_{oc}), in comparing with 16.43%, 64.35% and 1.05 V for control group (crystal tin oxide as ETL), respectively. Besides, the champion device keeps 83.33% of initial PCE under nitrogen (N_2) condition for one month, in comparison with 76.09% for control group. This work provides a viable strategy for facile preparing amorphous tin oxide film based ETL in perovskite solar cells.

Introduction

Organic–inorganic lead halide perovskite solar cells (PSCs) with planar regular (n-i-p) structure have achieved tremendous progress with enhancement of their power conversion efficiency (PCE) from 3.8% to 25.7%.[1–11] Especially, the electron transport layer (ETL) is a critical component to promote the transportation of photogenerated electrons and to block hole transportation in PSC device.[12–15] Tin oxide (SnO_2), a n-type of semiconductor, has become a desirable ETL material owing to its high optical transparency (~80%), unique band gap matching with lead-halide perovskite layer, high electron mobility up to 240 $cm^2\ V^{-1}\ s^{-1}$ and relatively low calcination temperature (100–500 °C) during its fabrication process.[16–22] Therefore, optimizing the fabrication strategy of the SnO_2 based ETL becomes a key factor to improve the PCE of PSCs device.

For low-temperature fabrication process, SnO_2 nanoparticles are often previously prepared using various ligand molecules, including tetramethylammonium hydroxide (TMAH), thiourea ($CS(NH_2)_2$), and urea ($CO(NH_2)_2$), to control the morphology of SnO_2 nanoparticles and to protect them from self-aggregation.[23–25] For instance, Fang *et al.*, designed thiourea as a capping ligand to prepare SnO_2 precursors with long time stirring up to 1–2 days before a spin-coating process to form SnO_2 in perovskite solar cells to acquire a 19.73% of PCE.[24] Hou *et al.*, prepared SnO_2 nanoparticle precursors mixed by $SnCl_2 \cdot 2H_2O$ and urea in deionized water and then stirring for 4–5 days at room temperature, resulting in 16.22% of PCE.[25] As a result, long ripen period up to several days is essential to fully obtain the SnO_2 nanoparticle precursor solution and their particle size depend on the ripen time at room temperature, causing the weakly repeatable results of PCE among batch of experiments. Therefore, exploring a novel fabrication method to bypass the SnO_2 nanoparticles precursor becomes challengeable to optimize the surface structure of SnO_2 based ETL.

In comparison with crystalline metal oxide films, amorphous semi-conductive metal oxide films exhibit comparable photoelectronic properties and can keep long-time work stability at elevated temperatures, owing to that amorphous film owns fewer inter-lattice spaces and less lattice disorder effects.[26] Amorphous metal oxide films have become promising alternatives in solar cell field. For example, Zhang *et al.*, fabricated an electron transport layer with amorphous structure of $InGaZnO_4$ to obtain a 9.07% of PCE in device of ITO/$InGaZnO_4$/$CsPbI_{1.2}Br_{1.8}$/C.[26] Kang *et al.*, modified amorphous SnO_2 nanoparticles onto crystalline SnO_2 to improve the PCE from 18.49% to 20.39%.[27] Especially, exploring a novel *in situ* one step growth strategy to fabricate amorphous SnO_2 film as ETL has rarely been explored, which may allow increased performance of lead-halide based PSCs.

Herein, this article uses $SnCl_2 \cdot 2H_2O$ as the tin source and *N*,*N*-dimethylformamide (DMF) as the solvent to realize *in situ*

National Engineering Research Center for Technology and Equipment of Green Coating, Lanzhou Jiaotong University, Lanzhou 730070, China. E-mail: 826634307@qq.com; clwang@lzjtu.edu.cn

† Electronic supplementary information (ESI) available. See DOI: https://doi.org/10.1039/d4ra01724b

one step growth of amorphous SnO_2 film at relative low annealing temperature (200 °C), as shown in Fig. 1a. The designed PSCs with structure of FTO/SnO_2/$MAPbI_3$/Spiro-OMeTAD/Ag owns a champion PCE up to 17.64%, comparing with 16.43% for control group (crystal tin oxide as ETL). The amorphous and crystal SnO_2 electron transport layers are denoted as Amo-SnO_2 and Con-SnO_2, respectively. The increased photo-electric efficiency and working stability of the designed PSC can be attributed to the utilization of amorphous SnO_2 as ETL through a facile one-step growth strategy to modulate the separation efficiency of photogenerated carriers and the elevated structure stability of amorphous SnO_2.

Experimental section

Experimental materials and reagents

Acetonitrile (ACN, 99.9%) and chlorobenzene (CB, 99.5%) were purchased from Sigma-Aldrich. *N*,*N*-dimethylformamide (DMF, 99.9%), dimethyl sulfoxide (DMSO, 99.8%), tin oxide powders (99.9%), anhydrous tin chloride (99.99%) and $SnCl_2 \cdot 2H_2O$ were obtained from Aladdin. Methyl iodide (MAI, 99.5%) was

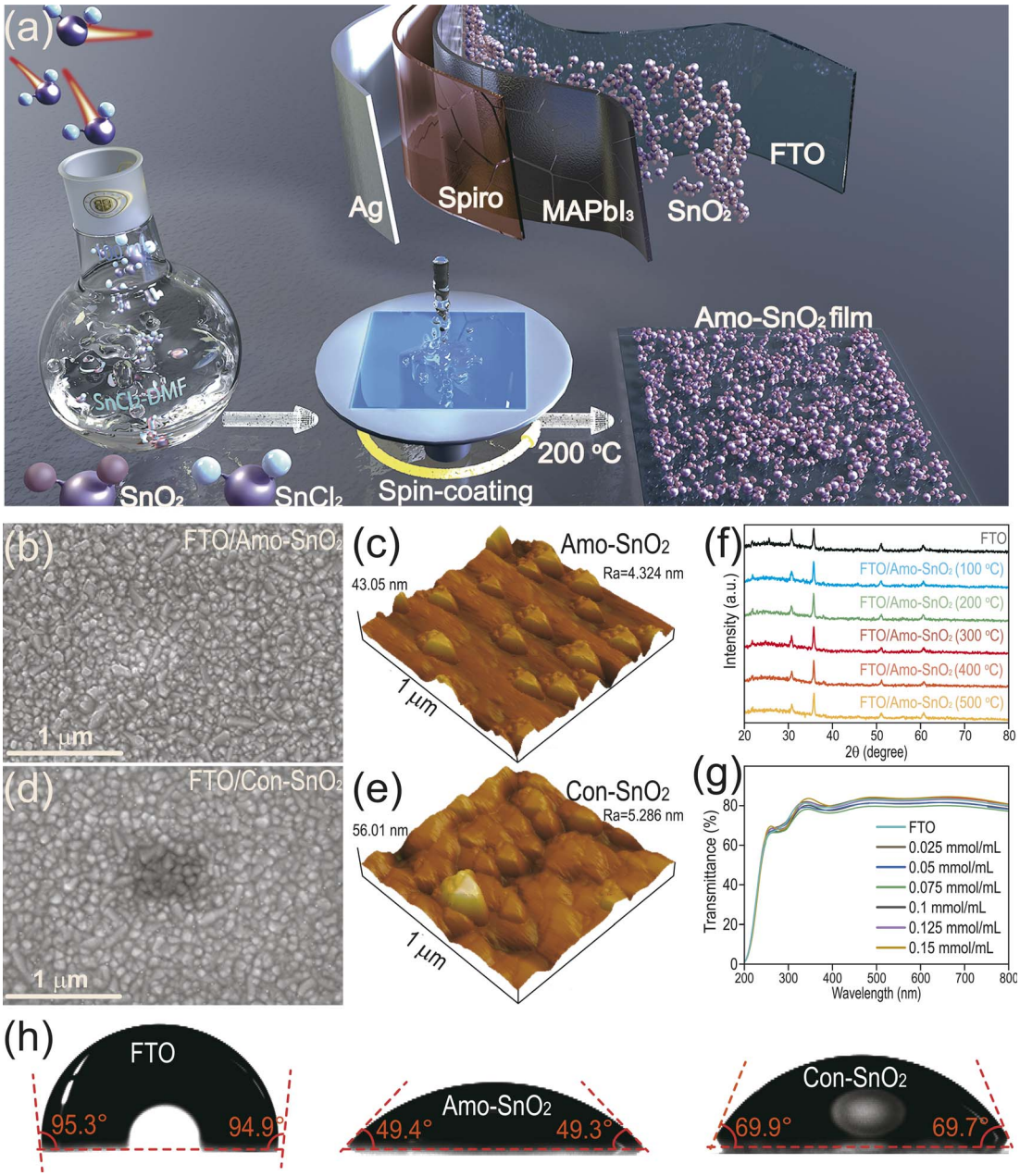

Fig. 1 (a) Schematic diagram of the proposed strategy for preparing Amo-SnO_2 film. SEM images of (b) Amo-SnO_2 and (d) Con-SnO_2 film by calcination at 200 °C. AFM images of (c) Amo-SnO_2 and (e) Con-SnO_2 film. (f) XRD patterns of the Amo-SnO_2 films at different calcination temperatures. (g) Optical Transmittance of Amo-SnO_2 films prepared with different concentrations of precursor solution and followed by calcination at 200 °C. (h) Contact angle images of SnO_2 films and FTO substrates.

purchased from Xi'an Yuri Solar Co., Ltd. Lead iodide (PbI_2, 99.9%), lithium bis (trifluoromethanesulfonyl) imide (Li-TFSI, 99.95%), 4-*tert*-butylpyridine (TBP, 96.0%) and 2,2′, 7,7′-tetrakis(*N*,*N*-di-*p*-methoxyphenylamine)-9,9-spirobifluorene (Spiro-OMeTAD, 99.86%) were purchased from Advanced Election Technology Co., Ltd. Fluorine-doped tin oxide glasses (FTO, 14 Ω, 1.5 × 1.5 cm) were purchased from Advanced Election Technology Co., Ltd. Ultrapure water with 18 MΩ was obtained from device of Ultrapure Water System (Corning Technology Development Co., Ltd, PRO-3200, Chengdu). All chemicals were used as achieved without further purification process.

Preparation of SnO_2 film

For amorphous SnO_2 film, the FTO substrates were cleaned consecutively with detergent, acetone, isopropanol, ethanol, and deionized water for 50 minutes through ultrasonic cleaning, and then dried at 75 °C in an air oven for several hours before the ozone treatment for 10 minutes. Subsequently, the $SnCl_2$ precursor was prepared by dissolving 22.5 mg of $SnCl_2 \cdot 2H_2O$ into 1 mL of DMF and stirring for 10 minutes at room temperature to form $SnCl_2$/DMF solution with concentration of 0.1 mmol mL^{-1}. Then, 35 μL of the $SnCl_2$ precursor solution was spin-coated onto cleaned FTO substrate at 3000 rpm for 30 seconds and followed by annealing at various temperatures from 100 to 350 °C for 1 hour to generate amorphous SnO_2 electron transport layer.

For crystal SnO_2 film (Con-SnO_2), 22.5 mg of $SnCl_2 \cdot 2H_2O$ was dissolved in 1 mL of ethanol to form the $SnCl_2$/ethanol solution with concentration of 0.1 mmol mL^{-1}. Then, the precursor solution was spin-coated onto clean FTO substrate with 3000 rpm for 30 s and followed by annealing at 180 °C for 1 h to obtain the Con-SnO_2 film.[20]

Preparation of perovskite solar cell device

The prepared SnO_2 electron transport layer was treated with ozone for 15 min prior to depositing perovskite precursor solution in order to remove organics on the surface of the SnO_2 electron transport layer. After that, 35 μL of perovskite precursor solution (containing the MAI and PbI_2 at 1 : 1 of stoichiometric ratio in a mixed solvent with $V_{DMF} : V_{DMSO} = 4 : 1$ to keep the concentrations of both MAI and PbI_2 at 1.25 mmol mL^{-1}) was dropped onto SnO_2 ETL film under conditions of 1000 rpm for 3 s and then 4000 rpm for 30 s and followed by dropping 200 μL of chlorobenzene at eighth second before annealing at 100 °C for 10 minutes. The hole transport layer (HTL) precursor solution was prepared by dissolving 17.5 μL of Li-TFSI acetonitrile (520 mg mL^{-1}) solution, 28.8 μL of tBP and 72.3 mg of Spiro-OMeTAD solution in 1 mL of chlorobenzene into a 2 mL of flask and followed by stirring for 12 hours at nitrogen atmosphere. Then, 20 μL of HTL precursor was spin-coated onto perovskite layer at 5000 rpm for 30 s and then ripened in a drying oven at room temperature overnight in air. Finally, Ag electrode with a thickness of ~100 nm was deposited onto the surface of the hole transport layer as the top electrode under vacuum condition with 4×10^{-3} Pa and a current of 40 A using a heating boat for 20 minutes.

Characterization of solar cell device

The photo-electric properties of prepared PSCs were analyzed by a standard solar cell device (San-EI Electric, XEC-300M2, Japan) equipped with a light source of atmospheric mass (AM) 1.5 G with 100 mW cm^{-2} of incident light power density. The effective testing area of the device was kept at 0.057 cm^2, and the test voltage was ranging from −0.2 to 1.2 V. Electrochemical workstation (ELS, CH Instruments, CHI 600D, China) was used for measuring the electrochemical AC impedance of PSCs, with 0.8 V of initial voltage, 1×10^6 Hz of high frequency and 1 Hz of low frequency. Other testing parameters including the amplitude and settling time were used based on the default values of workstation. Solar cell testing system (Desai Optoelectronics, 7-SCSpec IPCE, China) was employed for external quantum efficiency (EQE) analysis of PSCs device, with testing wavelength ranging from 300 to 800 nm.

Materials characterizations

X-ray diffraction meter (XRD, Bruker D8, Germany) was employed to analyze the crystal structure of films with scanning speed at 10° min^{-1}, step size at 0.026°, and scanning range from 20 to 80°. The absorption and transmission spectra of films were measured by an UV-Vis spectrophotometer (UV, Shimadzu, UV-1800, Japan) in a wavelength range of 500–1100 nm at room temperature. Fluorescence spectrophotometer (PL, Hitachi, F-7100, Japan) was used for testing the photoluminescence intensity of perovskite films with an excitation wavelength of 460 nm and emission wavelength from 650 to 850 nm. Scanning Electron Microscope (SEM, Hitachi, SU8020, Japan) was employed to observe the surface morphology of films. The electronic structure of prepared films was analyzed by X-ray photoelectron spectroscopy (XPS, Escalab, 250 Xi, America). Atomic Force Microscope (AFM, Shimadzu, SPM9700, Japan) was used for testing the surface roughness of films. Fourier Transform infrared spectroscopy (FTIR, Thermo Fisher, IS55, America) was used for analyzing the organic groups in films. The hydrophilicity of the films was measured by a video optical contact angle measuring instrument (CA, Dataphysics, OCA25, Germany). Valence band of films was calculated based on formula (1), where E_{VB} is valence band, φ is the work function of the XPS instrument (φ = 4.55 eV), $E_{VB,\ XPS}$ is the valence band position *versus* XPS. Defect state density is determined from formula (2), where ε is the vacuum dielectric constant, ε_0 is the relative dielectric constant, L is the thickness of the perovskite film, e is the elemental charge, V_{TFL} is the trap filling limit voltage at the transition point of the ohmic and trap filling limit regions, N_{trap} is the defect density of states.

$$E_{VB} = \varphi + E_{VB,\ XPS} - 0.44 \quad (1)$$

$$N_{trap} = \frac{2\varepsilon_0 \varepsilon V_{TFL}}{eL^2} \quad (2)$$

Results and discussion

The surface morphology of SnO_2 film

The entire process from preparing precursor solution of $SnCl_2$ to generating amorphous SnO_2 film is described in Fig. 1a. It is

noted that the stability of precursor solution plays a key role in obtaining the SnO_2 film with high quality and reproducible properties among batch of experiments. The prepared $SnCl_2$ precursor exhibits acceptable chemical stability with clear and transparent state up to six months in Fig. S1.† The SnO_2 film is then produced by spin coating of precursor solution at different annealing temperatures. In Fig. S2,† with increasing the annealing temperature more than 200 °C, the surface of the film becomes rough and appears obvious cracks, which is not beneficial to electron transfer and the growth of perovskite layer, caused by high annealing temperature leads to more oxygen defects and pinholes in the films.[28] Therefore, 200 °C is optimal to obtain SnO_2 film with high quality (denoted as Amo-SnO_2). The morphologies of Amo-SnO_2 and Con-SnO_2 films are then compared by scanning electron microscopy (SEM) and atomic force microscopy (AFM) in Fig. 1b–e and S3.† It can be seen that comparing with the Con-SnO_2 film, the Amo-SnO_2 film exhibits uniform and smooth surface covered onto FTO substrate, as demonstrated by the decreased surface roughness (R_a) of 4.324 nm for Amo-SnO_2 than that of 5.286 nm for Con-SnO_2 films. Then, XRD pattern demonstrates the amorphous structure of prepared SnO_2 film in Fig. 1f. There are no detectable characteristic peaks corresponding to standard SnO_2 with calcination temperature from 100 to 500 °C, indicating that the formation of amorphous structure of SnO_2 is independent of its calcination temperature. Similar results are also obtained when SnO_2 is covered onto glass substrate instead of FTO in Fig. S4.† Fig. S5† shows the XRD pattern of Con-SnO_2 thin film, the peak of Con-SnO_2 corresponds to the standard SnO_2: JCPDS SnO_2-PDF#41-1445. The formation of SnO_2 using ethanol is similar with using water as solvents to provide hydroxy group to form $Sn(OH)_2$. The function of DMF is possibly to form weak Sn–O–N bond instead of Sn–OH bond. The intermediate structure of Sn–O–N can inhibit the formation of crystal SnO_2, resulting in the amorphous SnO_2. For PSCs device, high optical transmittance of functional layers including HTL and ETL indicates less photons harvesting by functional layers and high photons utilization efficiency by active layers such as perovskite layer for improved performance of PSCs device. In Fig. 1g, the optical transmittance (300–800 nm) of Amo-SnO_2 films is optimized by modulating concentrations of $SnCl_2$ precursor. Up to 83.661% of optical transmittance is obtained with 0.1 mmol mL^{-1} of precursor solution. Identical result is also described by replacing FTO with glass substrates to obtain 88.782% of optical transmittance in Fig. S6.† The optimal optical transmittance of SnO_2 film is also demonstrated up to 82.874% at 200 °C of calcination temperature in Fig. S7.† Over high temperature (>200 °C) brings some micro-cracks on the surface of film, resulting in decreased optical transmittance. It is noted that hydrophilic surface of SnO_2 film can facilitate the adsorption and growth of perovskite film. Therefore, the surface hydrophilicity of SnO_2 films is evaluated by contact angle analysis in Fig. 1h. Decreased contact angle with 49.4° for Amo-SnO_2 than that with 69.9° for Con-SnO_2 indicates the enhanced hydrophilicity of Amo-SnO_2. Generally, surface roughness of film is positive correlated with its hydrophilic efficacy. However, for Amo-SnO_2, hydrophilic residual including chloride ion and DMF exist on the surface of film as demonstrated from Fig. 2c and S8,† resulting in the increased hydrophilic efficacy than that of Con-SnO_2. In addition, the growth process of Amo-SnO_2 film is analyzed by infrared spectroscopy tests in Fig. S8.† From the magnified FTIR spectra, trace of C–H and C=O groups can be detected in Amo-SnO_2-calcination, indicating the residual DMF on the surface of Amo-SnO_2 film. This result also demonstrates the *in situ* growth of Amo-SnO_2 film by converting $SnCl_2$-DMF into amorphous SnO_2 film.

Characterizations of electronic structure

X-ray photoelectron spectroscopy (XPS) is used to analyze the surface electronic structure of Amo-SnO_2 and Con-SnO_2 films. In Fig. S9,† detectable elements including Sn and O in both two kinds of films indicate the successful preparation of SnO_2 films without impurities. In Fig. 2a, it is found that there are peaks at 486.83 and 495.23 eV (corresponding to Sn $3d_{5/2}$) for Amo-SnO_2 and SnO_2 powder, respectively, indicating the existence of Sn^{4+} on the surface of Amo-SnO_2 film. Absence of Sn^{2+} is also demonstrated by the disappearance of peak at 486.0 eV for Amo-SnO_2. For SnO_2 film, the O 1s XPS (Fig. 2b) peaks at ~530.4 eV and ~531.8 eV can be attributed to Sn–O bond and hydroxyl (–OH) adsorbed on the surface of film, respectively.[21,22,29,30] The peak area ratio of Sn–O to hydroxyl for Amo-SnO_2 and Con-SnO_2 are calculated as 0.95 and 0.87, respectively, indicating the increased absorption of hydroxyl for Amo-SnO_2 than that for Con-SnO_2. Owing to the increased hydrophilic capability of Amo-SnO_2 over Con-SnO_2 (Fig. 1h), Amo-SnO_2 tends to absorb water molecule from air before XPS analysis. Increased hydrophilic surface of Amo-SnO_2 film exhibits advantage in depositing perovskite film toward high-performance PSCs. Compared with SnO_2 powder, the characteristic peaks of Sn 3d and O 1s of Amo-SnO_2 films exhibit minor shifts to high binding energy, which is caused by the residual chloride ions on its surface to passivate the vacancy of oxygen.[25,31] Besides, there exists Cl 2p peak for the Amo-SnO_2 (Fig. S9† and 2c), indicating the less amount of chloride ions on its surface. Comparing with $SnCl_2$ powder, the binding energy of Cl^- moves towards higher energy for Amo-SnO_2 film in Fig. 2c, which can be attributed to the formation of Sn–Cl bond, resulting in some oxygen vacancies existing on the surface.[31] Therefore, replacing the ethanol with DMF solvent can introduce less amounts of chloride ions on the surface of amorphous SnO_2 film. The presence of Cl^- contributes to growing perovskite films, passivating the defects at the interface of Amo-SnO_2 and perovskite, and inhibiting the non-radiative recombination of carriers.[32,33] It is noted that negligible difference for Sn 3d and O 1s spectra is found between Con-SnO_2 and SnO_2 powder, demonstrating that there is almost no Cl^- in Con-SnO_2 (Fig. 2a and b). Then, semiconductive properties of SnO_2 films are analyzed in Fig. 2d. Valence band is calculated based on formula (1) described in experimental sections. Similar valence bands are obtained for the Amo-SnO_2 (7.43 eV) and SnO_2 powder (7.23 eV). In contrast, higher band gap up to 3.63 eV is observed for Amo-SnO_2 than that for SnO_2 powder with 3.58 eV (Fig. 2e), possibly caused by the special amorphous structure of SnO_2. Besides, ultraviolet

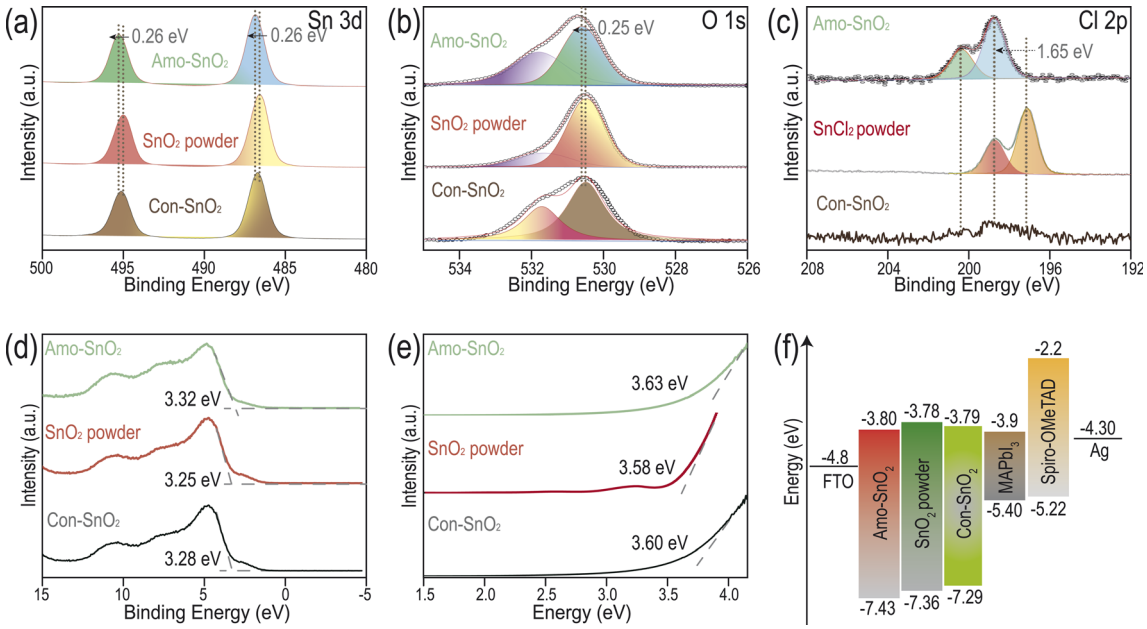

Fig. 2 High-resolution XPS spectra of SnO_2 based films: (a) Sn 3d, (b) O 1s, (c) Cl 2p. (d) Valence band spectra of films. (e) Bandgap diagram of films. (f) Energy level diagram of each layer in PSCs.

photoelectron spectroscopy (UPS) is performed to analyze the conduction bands of films in Fig. S10.† Combined with the band gap in Fig. 2e, the conduction band of the Amo-SnO_2 and Con-SnO_2 are determined as 3.8 and 3.79 eV. Finally, the energy levels of the Amo-SnO_2, SnO_2 powder, Con-SnO_2 and the perovskite active layer are described in Fig. 2f. This diagram indicates the appropriate conduction match between Amo-SnO_2 and perovskite active layer, promoting the extraction and transport of photo-generated electrons by active layer.

Characterizations of perovskite solar cell device

The morphologies of perovskite solar cell devices are characterized by SEM in Fig. 3a–d. Smooth and dense surface with larger grain size is observed for perovskite layer coated onto Amo-SnO_2 than that coating onto Con-SnO_2, which can promote the transfer of photo-generated electrons and reduce recombination of non-radiative charges. Cross-sections of PSCs are then explored in Fig. 3b and d. Dense contact between ETL and perovskite layers is obtained for Amo-SnO_2 and the thickness of each layer of the PSCs are determined as ~23 nm for Amo-SnO_2 (ETL), ~290 nm for $MAPbI_3$ (active layer), ~100 nm for Sprio-OMeTAD (HTL), and ~100 nm for Ag electrode, respectively. Besides, crystal structure of perovskite layers coated separately onto Amo-SnO_2 and Con-SnO_2 films are analyzed in Fig. S11.† The intensity of diffraction peak at 14.65° (corresponding to (110) plane) for Amo-SnO_2 is 1.45 times higher than that for Con-SnO_2 (Fig. S11†). Moreover, for Amo-SnO_2 films prepared at different annealing temperatures, 200 °C of annealing temperature results in higher crystallinity of $MAPbI_3$ in Fig. S12,† which is possibly caused by over high annealing temperature can deteriorate the surface structure of SnO_2. In Fig. 3e and f, increased optical absorption (380–760 nm) and decreased fluorescence emission intensity at 700 nm for perovskite layer coated onto Amo-SnO_2 layer are obtained than that onto Con-SnO_2 layer. Above results indicate that comparing with Con-SnO_2 layer, the Amo-SnO_2 layer is more suitable for growing perovskite with dense contact and high quality to provide higher electron extraction and transport efficacy with less non-radiation loss for high-performance device.

Performance of perovskite solar cell device

In order to further study the function of Amo-SnO_2 as an electron transport layer in perovskite solar cells, the n-i-p type of PSCs with structure of FTO/Amo-SnO_2/$MAPbI_3$/Spiro-MeOTAD/Ag are prepared. For Amo-SnO_2, the performance of PSCs is optimized by modulating the concentrations of precursor solutions of $SnCl_2$ and calcination temperature in Fig. S13 and S14.† The optimal parameters are kept at 0.1 mmol mL^{-1} of concentration and 200 °C of calcination temperature. Champion device with corresponding parameters including open circuit voltage (V_{oc}), short-circuit current density (J_{sc}), fill factor (FF) and photovoltaic conversion efficiency (PCE) are summarized in Tables S1 and S2.† In Fig. 4a, the photoelectric conversion efficiency (PCE) of using Amo-SnO_2 as ETL reaches up to 17.64%, which is significantly higher than that of using Con-SnO_2 as ETL PSCs (16.43% of PCE). This result is further demonstrated using batch of PSCs with twenty samples for PCE analysis by reverse scan in Fig. S15.† Average PCE for Amo-SnO_2 and Con-SnO_2 are 16.59 ± 0.59 and 15.34 ± 0.74, respectively. Forward and reverse scan of *J–V* curves are provided in Fig. S16.† For Amo-SnO_2, 15.44% and 17.38% of PCE are obtained for forward and reverse scan, respectively, comparing with the 13.87% and 16.19% for Con-SnO_2. Therefore, less hysteresis effect is obtained by Amo-SnO_2 than by Con-SnO_2 used as ETL in PSCs. To exploring the recombination of charge carriers occurring on the surface and inside of perovskite thin films, the

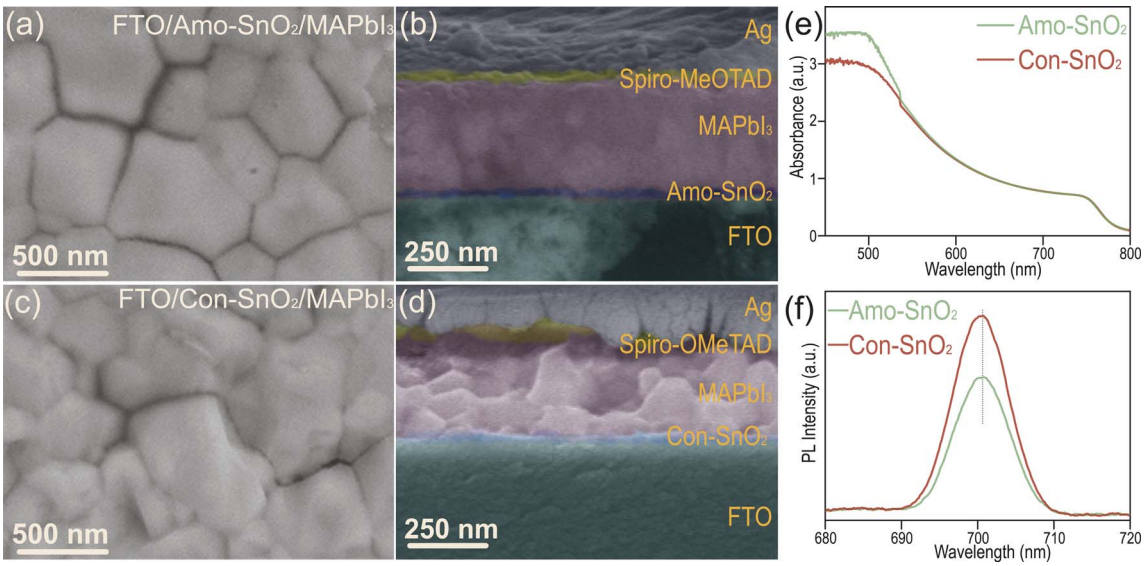

Fig. 3 SEM images of $MAPbI_3$ film coated onto (a)Amo-SnO_2 and (c) Con-SnO_2 films. Cross sections of PSCs using (b) Amo-SnO_2 and (d) Con-SnO_2 as ETL. (e) Ultraviolet visible absorbance and (f) PL spectra of perovskite films deposited separately onto Con-SnO_2 and Amo-SnO_2 layers.

external quantum efficiency (EQE) analysis is performed using the champion device. In Fig. 4b, the device of using Amo-SnO_2 as ETL owns higher optical response than that using Con-SnO_2 as ETL, resulting in increased J_{sc} of device using Amo-SnO_2 as ETL. The surface and internal defects of devices are evaluated by dark current density analysis. In Fig. 4c, dark current curve of

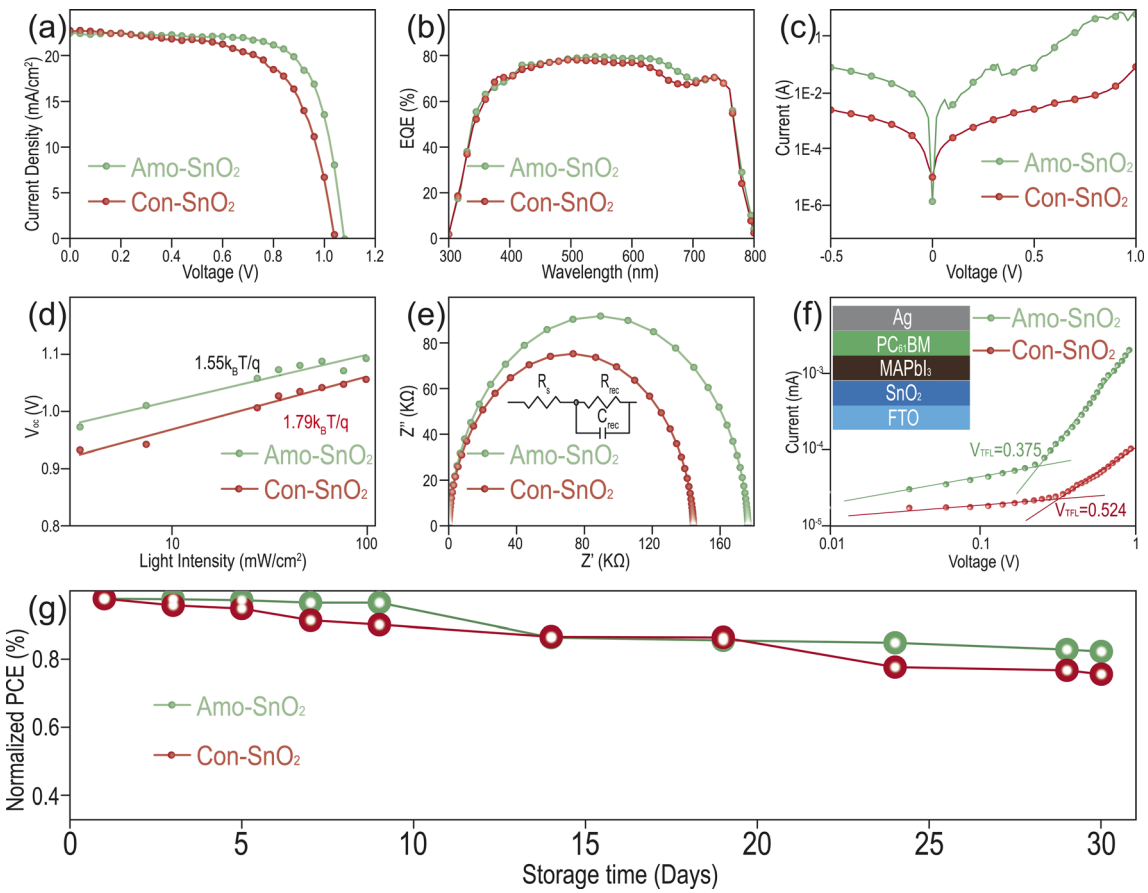

Fig. 4 (a) *J*–*V*, (b) EQE, (c) dark current density, (d) voltage changing with light intensity, (e) EIS in dark conditions at 0.8 V bias, (f) SCLC and (g) working stability curves of the devices using different electron transport layers.

device using Amo-SnO_2 as ETL indicates the decreased leakage current at the low-voltage scale, which suggests the dense interfacial contact between Amo-SnO_2 ETL and the active layer. Furthermore, photo-generated carrier recombination efficiency of device using various ETL can be illustrated by the light intensity and open circuit voltage curve in Fig. 4d. For PSCs with structure of FTO/SnO_2/$MAPbI_3$/Spiro-MeOTAD/Ag, Amo-SnO_2 exhibits smaller ideal factor (1.55) than Con-SnO_2 (1.79), indicating the suppression of non-radiative recombination, reduction and inhibition of V_{oc} losses and leakage current of PSCs using Amo-SnO_2 as ETL. Besides, the recombination of charge carriers in devices are analyzed using electrochemical impedance spectroscopy (EIS) in Fig. 4e. In the Nyquist plots, both devices using Amo-SnO_2 and Con-SnO_2 as ETL exhibit obvious semi-circular curves. Comparing with Con-SnO_2, device using Amo-SnO_2 as ETL obtains a larger semi-circular diameter, indicating higher composite resistance, larger composite resistance and lower probability of carrier recombination, which is beneficial for PSCs. To verify the carrier recombination of the device under light conditions, EIS map under light conditions are conducted in Fig. S17.† The composite resistance (R_{rec} = 52.48 kΩ) of Amo-SnO_2 is significantly higher than that of Con-SnO_2 (R_{rec} = 41.09 kΩ). In PSCs, higher R_{rec} and smaller R_s indicate lower carrier recombination and higher efficiency of extracting electrons, which is conducive to the performance of the PSCs. Combined EIS results under both light and dark conditions demonstrate weak carrier recombination efficiency when Amo-SnO_2 film is employed as ETL. In addition, the space charge limited current method (SCLC) is used to quantitatively characterize the defect state density of the PSCs. Defect densities of electrons are analyzed using the device without hole transport layer (FTO/SnO_2/$MAPbI_3$/$PC_{61}BM$/Ag). In Fig. 4f, the V_{TFL} of the champion device using Con-SnO_2 and Amo-SnO_2 as electron transport layers are 0.524 V and 0.375 V, respectively. The corresponding electrons trap densities (N_{trap}) using Amo-SnO_2 as ETL is obtained with 4.839×10^{15} cm^{-3}, which is significantly lower than that using Con-SnO_2 as ETL (6.762×10^{15} cm^{-3}). Finally, the long-term stability of the device is evaluated in Fig. 4g. After 30 days of storage, the device using Amo-SnO_2 as ETL still maintains 83.33% of the initial PCE in the glove box, in contrast with only 76.09% for Con-SnO_2, indicating the excellent stability of device using Amo-SnO_2 as ETL. Moreover, the prepared $SnCl_2$/DMF precursor also demonstrates long-time of stability over conventional $SnCl_2$/EtOH solution. In Fig. S18,† only 0.63% of PCE is reduced for Amo-SnO_2 after nine months of storage of $SnCl_2$/DMF solution at room temperature, in contrast with 1.85% of PCE reduction for Con-SnO_2 with identical treating process. Long time stability of PSCs using Amo-SnO_2 as ETL can be attributed to the special amorphous structure of SnO_2 favoring to maintain the long-time structure stability and keep dense contact between Amo-SnO_2 ETL and the active layer.

Conclusions

In summary, a facile *in situ* one step method is proposed for preparing amorphous SnO_2 film as the ETL. The as-synthesized Amo-SnO_2 film owns superior electrical conductivity, optimized band gap, and lower trap density compared with Con-SnO_2. The proposed method simplifies the preparation process of ETL in n-i-p type of device and extends the application of amorphous materials in PSCs. The device based on the Amo-SnO_2 thin film attains champion PCE up to 17.64% and 1.09 V of V_{oc}. In addition, the device using Amo-SnO_2 as ETL presents excellent stability up to 30 days with only 83.33% of reduction of initial PCE. Finally, this work provides a viable method for the application of amorphous electron transport layers in perovskite solar cells.

Author contributions

The manuscript was written through contributions of all authors. All authors have given approval to the final version of the manuscript.

Conflicts of interest

The authors declare no conflict of interest.

Acknowledgements

This work is supported by Major Cultivation Project of Gansu Province University Research and Innovation Platform (2024CXPT-03); The financial support of this work was provided by Gansu Provincial Natural Science Foundation of China (6B0023); Science Foundation of Lanzhou Jiaotong University (1200061037); Gansu Provincial Department of Education: Major Cultivation Project for College and University Scientific Research Innovation Platforms (2024GJPT-01).

Notes and references

1 A. Kojima, K. Teshima, Y. Shirai and T. Miyasaka, *J. Am. Chem. Soc.*, 2009, **131**, 6050–6051.
2 H. P. Zhou, Q. Chen, G. Li, S. Luo, T. B. Song, H. S. Duan, Z. Hong, J. B. You, Y. S. Liu and Y. Yang, *Science*, 2014, **345**, 542.
3 J. Song, W. N. Zhang, D. Wang, K. M. Deng, J. H. Wu and L. Zhang, *Sol. Energy*, 2019, **185**, 508–515.
4 M. M. Hu, L. Z. Zhang, S. Y. She, J. C. Wu, X. Y. Zhao, X. G. Li, D. Wang, J. Miao, G. J. Mi, H. Chen, Y. Q. Tian, B. M. Xu and C. Cheng, *Sol. RRL*, 2020, **4**, 1900331.
5 Q. Jiang, Z. M. Chu, P. Y. Wang, X. L. Yang, H. Liu, Y. Wang, Z. G. Yin, J. L. Wu, X. W. Zhang and J. B. You, *Adv. Mater.*, 2017, 1703852.
6 C. Luo, G. H. J. Zheng, F. Gao, X. J. Wang, C. L. Zhan, X. Y. Gao and Q. Zhao, *Nat. Photonics*, 2023, **17**, 856–864.
7 Q. Jiang, L. Q. Zhang, H. L. Wang, X. L. Yang, J. H. Meng, H. Liu, Z. G. Yin, J. L. Wu, X. W. Zhang and J. B. You, *Nat. Energy*, 2017, **2**, 16177.
8 N. J. Jeon, J. H. Noh, W. S. Yang, Y. C. Kim, S. C. Ryu, J. W. Seo and S. I. Seok, *Nature*, 2015, **517**, 476–480.
9 W. S. Yang, J. H. Noh, N. J. Jeon, Y. C. Kim, S. C. Ryu, J. W. Seo and S. I. Seok, *Science*, 2015, **348**, 1234–1237.

10 N. X. Li, S. X. Tao, Y. H. Chen, X. X. Niu, C. K. Onwudinanti, C. Hu, Z. W. Qiu, Z. Q. Xu, G. H. J. Zheng, L. G. Wang, Y. Zhang, L. Li, H. F. Liu, Y. Z. Lun, J. W. Hong, X. Y. Wang, Y. Q. Liu, H. P. Xie, Y. L. Gao, Y. Bai, S. H. Yang, G. Brocks, Q. Chen and H. P. Zhou, *Nat. Energy*, 2019, **4**, 408–415.

11 M. H. Li, J. J. Zhou, L. G. Tan, H. Li, Y. Liu, C. F. Jiang, Y. R. Ye, L. M. Ding, W. Tress and C. Y. Yi, *Int. J. Innov.*, 2022, **3**, 100310.

12 H. Min, D. Y. Lee, J. Kim, G. Kim, K. S. Lee, J. Kim, M. J. Paik, Y. K. Kim, K. S. Kim, M. G. Kim, T. J. Shin and S. I. Seok, *Nature*, 2021, **598**, 444–450.

13 Y. C. Chen, Q. Meng, L. R. Zhang, C. B. Han, H. L. Gao, Y. Z. Zhang and H. Yan, *J. Energy Chem.*, 2019, **35**, 144–167.

14 L. Y. Lin, T. W. Jones, T. C. J. Yang, N. W. Duffy, J. H. Li, L. Zhao, B. Chi, X. B. Wang and G. J. Wilson, *Adv. Funct. Mater.*, 2020, **31**, 2008300.

15 K. Valadil, S. Gharibi, R. T. Ledari, S. Akin, A. Maleki and A. E. Shalan, *Environ. Chem. Lett.*, 2021, **19**, 2185–2207.

16 L. J. Zuo, H. X. Guo, D. W. deQuilettes, S. Jariwala, N. D. Marco, S. Q. Dong, R. DeBlock, D. S. Ginger, B. Dunn, M. K. Wang and Y. Yang, *Sci. Adv.*, 2017, **3**, e1700106.

17 J. S. Xie, K. Huang, X. G. Yu, Z. R. Yang, K. Xiao, Y. P. Qiang, X. D. Zhu, L. B. Xu, P. Wang, C. Cui and D. Yang, *ACS Nano*, 2017, **11**, 9176–9182.

18 Z. P. Wang, Q. Q. Lin, F. P. Chmiel, N. Sakai, L. M. Herz and H. J. Snaith, *Nat. Energy*, 2017, **2**, 17135.

19 W. J. Ke, D. W. Zhao, A. J. Cimaroli, C. R. Grice, P. L. Qin, Q. Liu, L. B. Xiong, Y. F. Yan and G. J. Fang, *J. Mater. Chem. A*, 2015, **3**, 24163–24168.

20 W. J. Ke, G. J. Fang, Q. Liu, L. B. Xiong, P. L. Qin, H. Tao, J. Wang, H. W. Lei, B. R. Li, J. W. Wan, G. Yang and Y. F. Yan, *J. Am. Chem. Soc.*, 2015, **137**, 6730–6733.

21 J. J. Zhang, H. Y. Wang, Q. Y. Yang, C. Gao, C. X. Gao and X. Z. Liu, *Opt. Mater.*, 2023, **137**, 113518.

22 M. Shi, T. C. Bai, S. S. Du, H. M. Sha, H. Chen, X. H. Ma, Y. D. Xu and Y. Q. Chen, *Acta*, 2023, **444**, 141985.

23 Z. L. Zhu, Y. Bai, X. Liu, C. C. Chueh, S. H. Yang and A. K. Y. Jen, *Adv. Mater.*, 2016, **28**, 6478–6484.

24 G. Yang, C. Chen, F. Yao, Z. L. Chen, Q. Zhang, X. L. Zheng, J. J. Ma, H. W. Lei, P. L. Qin, L. B. Xiong, W. J. Ke, G. Li, Y. F. Yan and G. J. Fang, *Adv. Mater.*, 2018, **30**, 1706023.

25 H. R. Tian, J. J. He, X. Y. Liu, Q. Li, D. Liu, B. B. Shen, S. Yang, Q. Niu and Y. Hou, *Small Sci.*, 2023, **3**, 2200112.

26 C. Zhang, X. T. Yin, Y. X. Guo, H. X. Xie, D. Liu and W. X. Que, *Phys. Chem. Chem. Phys.*, 2022, **24**, 18896.

27 H. B. Lee, N. Kumar, M. M. Ovhal, Y. J. Kim, Y. M. Song and J. W. Kang, Dopant-Free, *Adv. Funct. Mater.*, 2020, **30**, 2001559.

28 W. Ke, D. Zhao, A. J. Cimaroli, C. R. Grice, P. Qin, Q. Liu, L. Xiong, Y. Yan and G. Fang, Effects of annealing temperature of tin oxide electron selective layers on the performance of perovskite solar cells, *J. Mater. Chem. A*, 2015, **3**, 24163.

29 S. W. Shi, J. L, T. l. Bu, S. L. Yang, J. Y. Xiao, Y. Peng, W. Li, J. Zhong, Z. L. Ku, Y. B. Cheng and F. Z. Huang, *RSC Adv.*, 2019, **9**, 9946–9950.

30 J. Li, T. L. Bu, Y. F. Liu, J. Zhou, J. L Shi, Z. L. Ku, Y. Peng, J. Zhong, Y. B. Cheng and F. Z. Huang, *ChemSusChem*, 2017, **11**, 2898–2903.

31 J. W. Liang, Z. L. Chen, G. Yang, H. B. Wang, F. H. Ye, C. Tao and G. J. Fang, *ACS Appl. Mater. Interfaces*, 2019, **11**, 23152–23159.

32 P. Y. Wang, B. B. Chen, R. J. Li, S. L. Wang, N. Y. Ren, Y. C. Li, S. Mazumdar, B. Shi, Y. Zhao and X. D. Zhang, *ACS Energy Lett.*, 2021, **6**, 2121–2128.

33 J. B. Wu, C. Zhen and G. Liu, *Rare Met.*, 2022, **41**, 361–367.